Supplementary Material for *Controlled suppression of superconductivity by the generation of polarized Cooper pairs in spin valve structures* by *M.G. Flokstra et al.*

This *Supplementary Material* contains additional discussion on the growth and characterisation of the samples discussed in the manuscript. While not essential to the understanding or conclusions of the manuscript, specialist readers may find the additional material useful and informative.

1. Sample Design and Preparation

Here we provide further details on the sample design, preparation and characterisation.

1.1 Sample Design

The basis for the SFF and FSF structures used in this work are conventional bottom-pinned exchange biased thin-film spin valve structures. The generic structure is antiferromagnet (AF)/pinned ferromagnet (F_1)/spacer/free ferromagnet (F_2) and cap layer where exchange bias between the anti-ferromagnet and pinned ferromagnet gives a unidirectional anisotropy to the pinned ferromagnet, whilst the free ferromagnetic layer lacks this strong anisotropy and id decoupled from the pinned layer by the spacer.

The two structures differ in the relative thickness of the spacer and cap layers, with the SFF structure having a thin (3 nm) Nb spacer and thick (50 nm) Nb cap, whilst the FSF has a thick (50 nm) Nb spacer and no Nb cap layer. In all cases the ferromagnetic layers are Co due its comparatively long spin diffusion length.

The full sample stacks were thus, Au(6)/Nb(50)/Co(1.6)/Nb(3)/Co(0.8)/ IrMn(4)/Co(3)/Ta(7.5)/Si-substrate for the SFF structure and Au(6)/Co(2.4)/Nb(50)/Co(1.2)/ IrMn(4)/Co(3)/Ta(7.5)/Si-substrate, where the numbers in brackets are the thicknesses of the corresponding layers in nm. In order for the antiferromagnetic IrMn layer to exchange bias the thin (1.2 nm) Co pinned layer, it was necessary to deposit the IrMn on a magnetically saturated ferromagnetic interface or, alternatively, for the whole sample stack to be annealed above the Neel temperature of the IrMn in a saturating magnetic field. Since this latter process could potentially cause inter-diffusion of the layers at the critical interfaces, the former approach was used and so below the antiferromagnetic IrMn layer we first deposited a 3 nm Co buffer layer. During the deposition a homogenous magnetic field is applied in the plane of the samples and this ensures that the lowest buffer Co layer is saturated. The lowest Ta layer acts as a buffer to provide a textured surface to promote the growth of the subsequent magnetic layers. The final 6 nm Au layers serve as a cap to prevent oxidation of the stack after growth.

1.2 Sample Preparation

Samples were prepared by dc magnetron sputtering on Si (100) substrates in a system with a base pressure of 10^{-8} mbar. During growth substrates were at ambient temperature and growth was carried out in a single vacuum cycle at a typical Ar flow of 24 sccm and pressure of 2-3 μbar and a substrate-sample distance of approximately 25 mm, with a typical growth rate of 0.2 nms^{-1}. Growth rates for each material were calibrated using fits to the Kiessig fringes in low angle X-ray reflectivity measurements of single layers of each material. The superconducting critical temperature of Nb is strongly dependent on vacuum conditions and is also thickness dependent for films less than 50 nm thick. Separate single films of Nb were grown in the same vacuum cycle as the samples and typically had a critical temperature of ~8.5 K for a 50 nm film.

2. Scanning Hall probe microscopy

Here we introduce the technique of scanning Hall probe microscopy and presents the key experimental conclusions of the measurements made in support of the above manuscript.

2.1 Introduction to the Technique

Scanning Hall probe microscopy is a quantitative and non-invasive magnetic imaging technique for measuring the local *perpendicular* component of surface magnetic fields on a sub-micrometer lengthscale. Measurements are based on a cross-shaped Hall effect sensor patterned in the two-dimensional electron gas (2DEG) of an AlGaAs/GaAs heterostructure wafer using electron-beam lithography and wet chemical etching. After accounting for side wall depletion of carriers we estimate that the width of the active sensor region is 0.6μm. The large Hall coefficient ($R_H = 1/n_{2D}e \approx 0.3\Omega G^{-1}$) and high mobility of the 2DEG at low temperatures ($\mu \approx 100 m^2V^{-1}s^{-1}$) make it an excellent material for the fabrication of Hall effect sensors and affords minimum detectable fields of ~$2mGHz^{-0.5}$. The Hall probe (HP) is mounted on a piezoelectric scanner tube which allows *fine* nanoscale motion in x-y-z. The piezotube is itself mounted inside a piezoelectric "slip-stick" motor which enables *coarse* motion perpendicular to the sample plane (z-direction). The sensor is approached towards the sample in coarse steps, after each of which the scanner piezotube fully extends and searches for a tunnel current via an integrated scanning tunnelling tip (STM) that is fabricated ~5μm from the HP. If no tunnel current is detected the piezotube fully retracts, another coarse approach step is made and the cycle continues until tunnelling is detected. To facilitate the detection of a tunnel current the sample is held at a small voltage bias (~0.2V), and the tilt angle between sensor and sample is set to ~1-2° to ensure that the STM tip always comes into contact with the surface of the sample first.

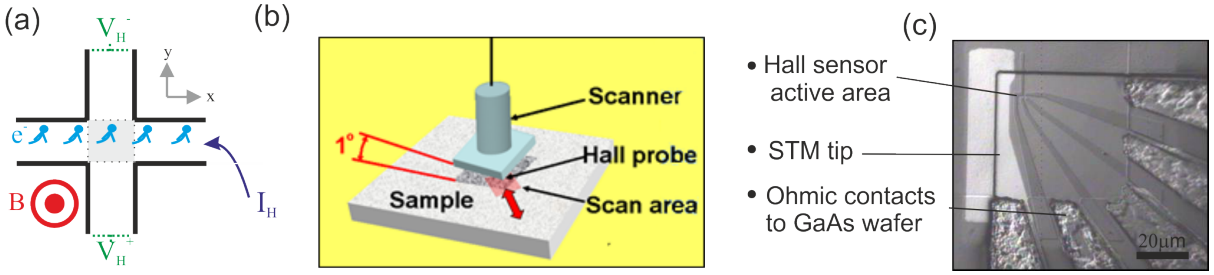

Fig. 1. Schematics of the cross-shaped Hall effect sensor (a) and the sample/sensor alignment (b). An optical micrograph of a sub-micron Hall probe fabricated in an AlGaAs/GaAs heterostructure wafer (c).

Once tunnel contact is established the sensor is retracted a small distance (~200nm) from the sample, and scanned at ~0.5Hz to build up 128 x 128 pixel two-dimensional maps of the local magnetic induction. The temperature dependent scan size is ~$57x57\mu m^2$ at 300K, ~$20x20\mu m^2$ at 77K, ~$8x8\mu m^2$ at 4.2K.

The whole microscope head sits in Helium exchange gas in a commercial variable temperature insert (VTI) of a ^{4}He cryostat which allows control of the temperature between ~300K and 4.2K. External in-plane magnetic fields are applied via a room temperature electromagnet that sits on a turntable that allows 360°rotation in the sample plane.

2.2. SHPM measurements of the stray fields at the surface of thin-film spin valve devices.

In addition to imaging in constant applied fields, the microscope can also be used to perform static measurements of the local magnetic induction by parking the HP at a fixed location and sweeping the applied field around a hysteresis loop. Figure 2 shows the perpendicular magnetisation measured above a *control sample* when sweeping the in-plane field *collinear* to the pinning direction. This control sample contains only the lower half of the spin valve structure, comprising the IrMn antiferromagnetic pinning layer sandwiched between the two *pinned* ferromagnetic layers: the Co buffer layer underneath and the active pinned F layer on top (see SI Section 1.1). There is thus no free layer or superconducting layer. Comparison with the SQUID data of the same sample (inset of Fig. 2 of the manuscript and Fig. 6 of the SI) shows that the spikes observed in the 'local' out-of-plane magnetization, M_z, at $\mu_0 H_a \approx -40$ mT and $\mu_0 H_a \approx -50$ mT correspond to the switching of the pinned "buffer" layer. A sequence of SHPM images taken at the fields indicated in Fig. 2(a), is also presented. Fig. 2(b) illustrates that even at zero applied field, a weak magnetic contrast is visible. Here, darker areas represent regions where flux is directed "down" away from the HP, and lighter areas are where stray fields are pointing "up" out of the sample plane, towards the HP. The perpendicular stray field presumably results from sample inhomogeneities arising from the polycrystalline IrMn antiferromagnetic layer.

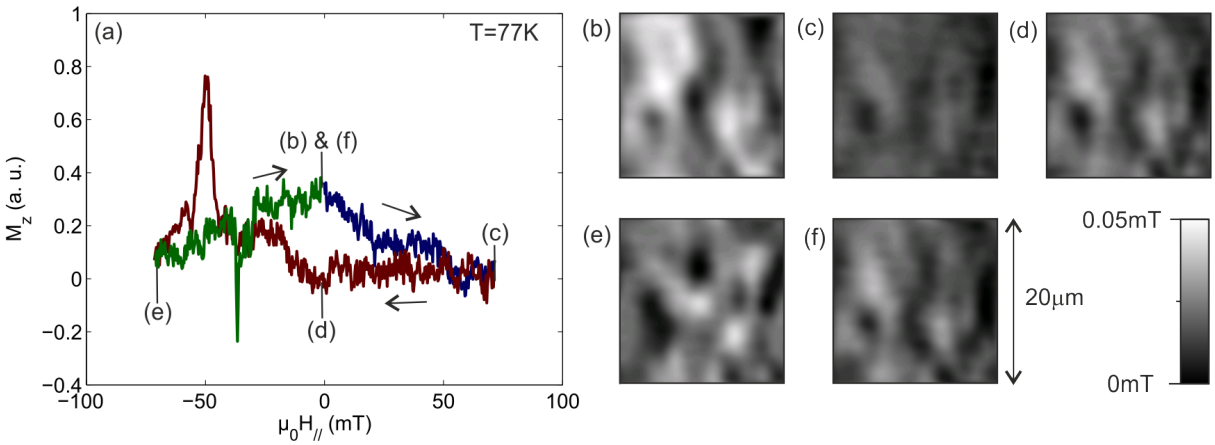

Fig. 2. (a) 'Local' magnetisation loop at a fixed position on the control sample at 77K. (b)-(f) SHPM images at the fields indicated in (a). The applied field is collinear with the exchange biased pinned moment.

The distribution of the stray fields remains approximately constant as the in-plane applied field is swept out to $\mu_0 H_a$=+70mT and back to zero ((b) to (d)). The amplitude of the stray fields drops significantly as the magnetisation becomes more saturated at $\mu_0 H_a$=+70mT and the moments are increasingly trained in the applied field direction. At $\mu_0 H_a$=-70mT (e) the image contrast undergoes a qualitative change when the pinned "buffer" moment reverses direction. Hence *we establish a clear link between contrast in the image and the microscopic magnetisation distribution of the Co layer.* At the end of the loop, the initial field distribution is recovered, indicating that the Co moment has reversed back to its original direction under the exchange bias field.

Figure 3 shows SHPM images of the same control sample with an in-plane field ($\mu_0 H_a$=20mT), that was originally collinear with the pinned moment (a), and is smoothly rotated out to 90° (c). There is no discernible change to the flux distribution during this

rotation and we conclude that *the pinned moments of the control sample are largely unaffected by a rotating in-plane field of this magnitude*.

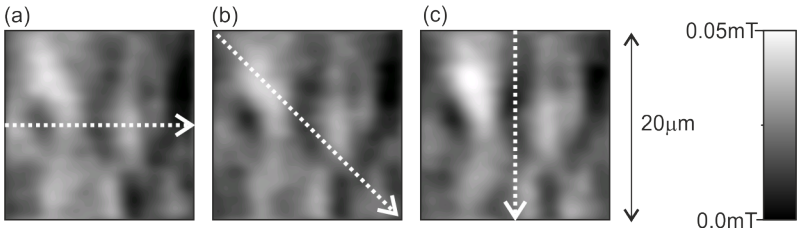

Fig. 3. SHPM images of the control sample at T=77K, after rotation of a $\mu_0 H_a$=20mT in-plane field that is (a) initially collinear with, (b) 45° and (c) perpendicular to the exchange biased moment, as indicated by the dashed arrows.

Figure 4 shows the 'local' perpendicular magnetisation, M_z, of a full SFF spin valve device (sample C in the manuscript) during a sweep of a collinear in-plane field while the HP is parked in the centre of the field-of-view. The two sharp and symmetrical switching events observed at $\mu_0 H_a \approx \pm 1.5$mT correspond to the reversal of the *free* Co layer. SHPM images of the remanent state taken at zero field after saturation in the *anti-parallel* (b) and *parallel* (c) directions illustrate how the background domain structure reverses contrast when the free layer moment is flipped 180°.

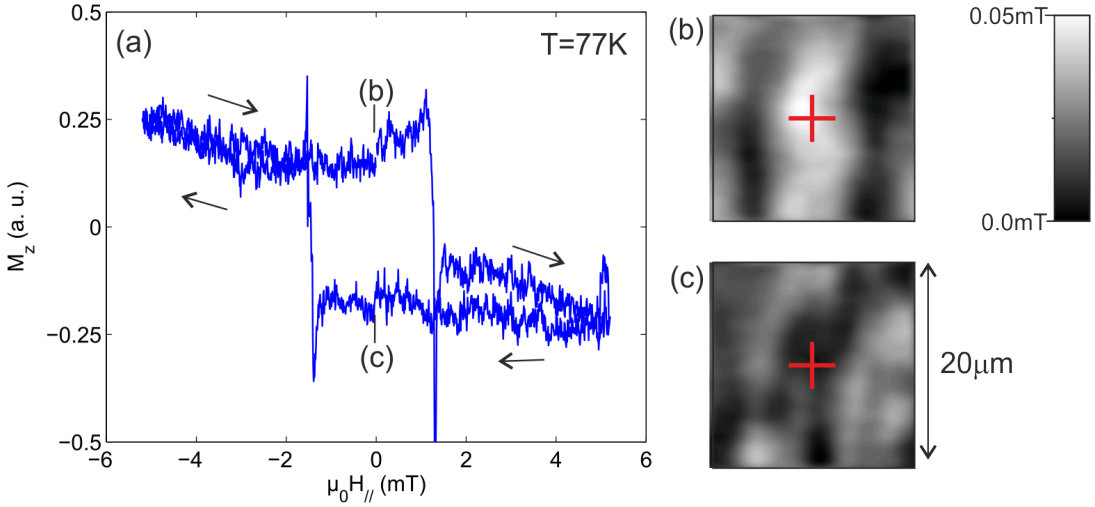

Fig. 4. The 'local' perpendicular magnetisation versus in-plane field above a full SFF spin valve device (sample C). The applied field is collinear with the pinned moment. SHPM images show the remnant magnetisation after saturation in the anti-*parallel* (b) and *parallel* (c) directions. Crosses in the images indicate the position of the HP during the sweep in (a).

Figure 5 shows SHPM images of the SFF sample C at 5K, when the free layer moment is rotated from parallel (θ_{Ha}=0°) to perpendicular (θ_{Ha}=90°) with respect to the pinned moment by an applied in-plane field of $\mu_0 H_a$=10mT, (a) and (b) respectively. The stray field pattern is *independent of the direction of in-plane field* for $T<T_c$ of the S layer. The stray fields at the surface of our samples are therefore very small (<0.5G) and, at low temperatures ($T<T_c$) these do not change appreciably as the free moment is rotated.

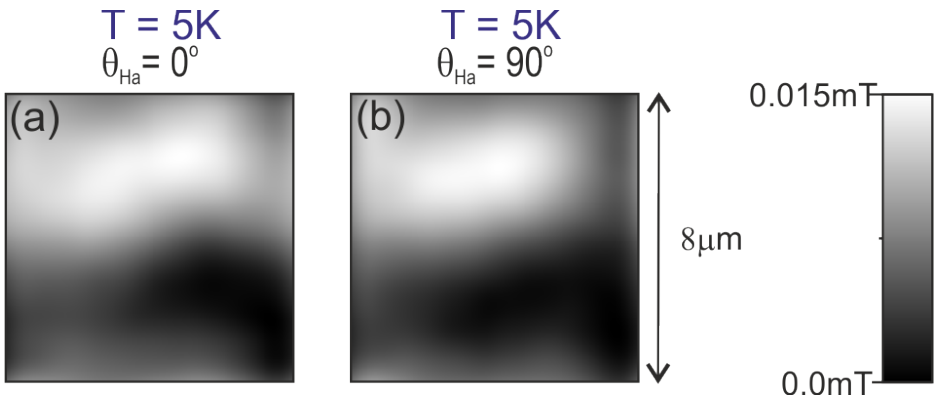

Fig. 5. SHPM images of stray fields at the surface of the SFF spin valve (sample C) under rotation of the free layer in an applied field of $\mu_0 H_a$=10mT ($T<T_c$), rotated from parallel with the pinned moment ((a) θ_H=0°) to perpendicular ((b) θ_H=90°).

In conclusion, it is clear that the observed stray fields from both the pinned layer and free layers are *very small*. Moreover, under the conditions of the experiment, the domain patterns that are observed *do not show any appreciable variation with the in-plane angle* of the applied field. It follows that this is also true for the angle between the pinned and unpinned components of the spin valve. *Any angular dependent variations we observe in transport data can thus not be attributed to changing stray field patterns or domain structures*.

3. Magnetisation Measurements of the Switching of the Active Pinned Co Layer

Here we present additional magnetisation data to that presented in Fig.1 of the manuscript. The latter focussed on the field range relevant to the switching of the free F layer, and also included switching data on the Co buffer layer located below the IrMn antiferromagnetic layer. He we extend the range of measurement field to show that the active pinned F layer is strongly pinned until much high fields, well above any fields applied during the experiment.

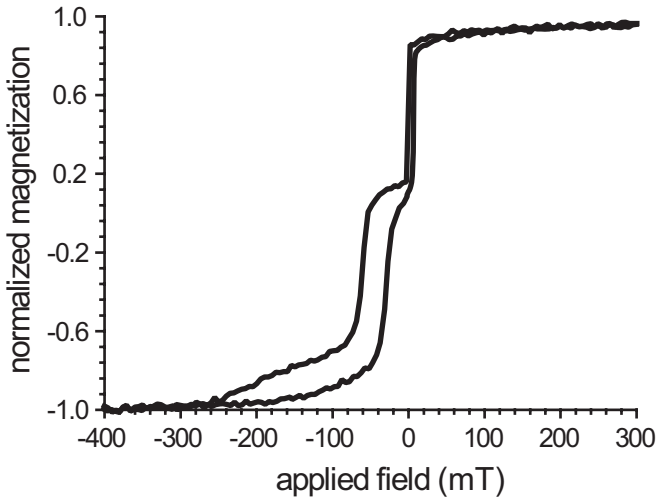

Fig. 6. VSM magnetisation data on a typical spin valve structure used in the transport measurements. The field is applied along the exchange bias direction.

The sharp switching close to zero applied field is due to the free F layer. One further reversing the field the Co buffer layer under the IrMn switches. Finally the pinned active F layer reverse, which does not fully saturate until fields in excess of 0.25T.

4. Variation of T_c as a Function of Angle

Here we present the variation of the critical temperature as function of the angle between the exchange directions of the Co layers and compare results with theory.

4.1 Converting the Angular Resistance Data to Variations in T_c

In Fig. 1 of the manuscript we present resistance as a function of temperature through the transition to the superconducting state, for both collinear and orthogonal arrangements of the magnetic layers in the spin valve. Thereafter we present measurements of the resistance of the sample as a function of the angle of the field to the pinned layer (effectively equal to the mutual angle of the magnetic layers). These measurements are taken at a selection of points within the superconducting transition. We prefer to present the data in this way since it reflects the way in which the experiments were undertaken. One can estimate the T_c shift as function of angle (α) from the angular dependent resistance data using a well determined R(T) curve. The main assumption to make however is that the shape of the R(T) curve does not change as function of α. Taking the R(T) curve at α=0 as reference one can write R(T+dT(α),0) = R(T,α); the resistance at temperature T and angle α, R(T,α), is identical to the reference curve R(T,0) shifted along the temperature axis by dT(α). The validity of this assumption is however questionable and in our spin-valve we typically find an increasing shift towards the lower sections of the R(T) curve (see Fig.1)). It is nonetheless worth doing this conversion for comparison with other works where this approach has been adopted. If we were to define the T_c shift in Fig.1 at the midway point: $R(T_c) = 0.5*R_{10,}$ then we would find a T_c shift of ~10mK between the collinear and orthogonal arrangement. However, this increases up to about ~15mK at the lowest section of the R(T) curve where $R(T_c) \sim 0$. While this might be expected to only result in a different scaling factor for the derived $T_c(\alpha)$ we find that data taken at the lowest sections of the R(T) curve, where the resistance in the collinear states is zero, start to smoothen out the sharp cusps at collinear angles. This is shown in Fig.7 where two $T_c(\alpha)$ curves are presented for α=-30 to α=210, both obtained on the FSF layout and both scaled to a maximum Tc shift of 10 mK. The left panel is derived from data taken near the midway point of the transition curve and shows clear cusps and follows a |sin| functional form. The right panel is derived from data taken at a very low section of the R(T) curve and shows a strong rounding of the cusps near the collinear angles.

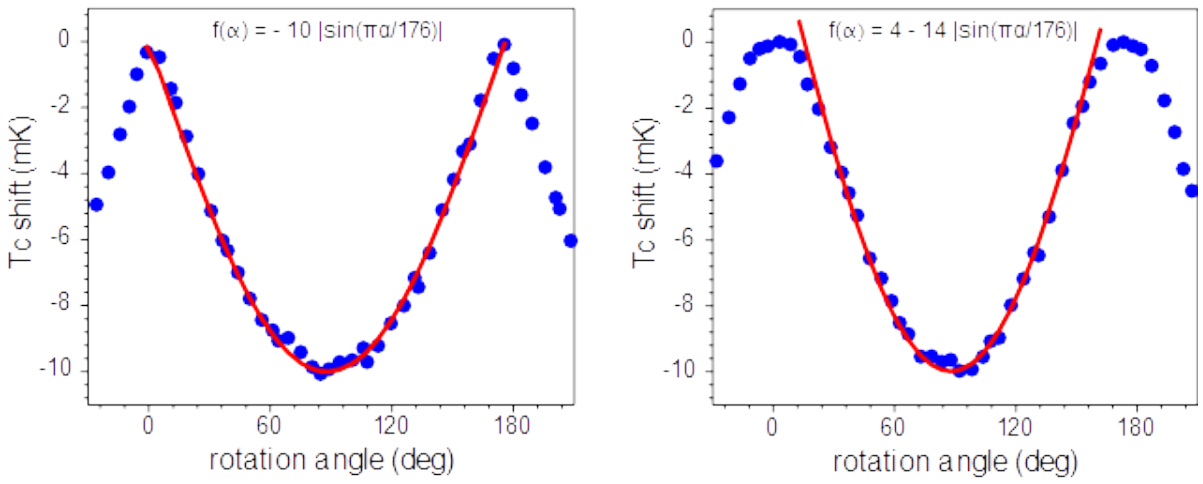

Fig. 7. The shift in the superconducting transition temperature T_c as a function of the mutual angle of the magnetic layers of the FSF spin valve. The zero angle corresponds to the field applied along the exchange bias direction and both are scaled to a maximum shift of 10mK. Left panel: data taken near the midway point of the transition curve. Right panel: data taken near the lowest section of the transition curve.

4.2 Theoretical Modelling of the Angular Variations in T_c

We calculate the angular dependence of the T_c shift in the clean limit by linearizing the Bogoliubov-de Gennes equations and looking for the highest temperature that yields a non-vanishing pair potential $\Delta(z)$. The formalism used here is the same as the one introduced by Barsic, Valls, and Halterman [Phys. Rev. B 75, 104502 (2007); Phys. Rev. Lett. 105, 207002 (2010)]. When the temperature of the system is just below the critical temperature, the pair potential can be treated as a small parameter and the corresponding self-consistent equation for $\Delta(z)$ can be linearized. This yields an eigenvalue problem for the Fourier components Δ_k of the pair potential, $\Delta_k = \Sigma_l (J_{kl} \Delta_l)$, where the matrix elements J_{kl} are temperature dependent. The critical temperature is then given by the highest temperature for which the largest eigenvalue of J is greater than or equal to unity.

Calculated shifts in T_c for an FSF structure with the same geometrical parameters as the ones of our Sample B are shown in Fig.8 and compared to the derived $T_c(\alpha)$ curve from Fig.7 originating from data taken at the lowest temperature (right panel). The choice for the curve obtained at the lowest section of the transition curve is because theory and experiment are then in closest agreement. This is because the non-zero pair potential obtained by theory should give a zero resistance path when measured, so the closer the original $R(\alpha)$ curve is to zero the better the expected agreement should be. The difference between the two fit curves is related to a different choice in the set of phenomenological parameters that characterize the materials. One uses for Nb a ratio of Debye temperature over Fermi temperature of $T_D/T_F = 0.04$ and a dimensionless superconducting coupling $\lambda = 0.7$, whereas the other used $T_D/T_F = 0.05$ and $\lambda = 0.5$. In both cases the Co layers are assumed to be strong ferromagnets with exchange energy $h = 0.5\ E_F$. Although the curves have slightly different functional behaviour, it is worth stressing that that they both show a suppression of T_c due to non-collinearity that has a minimum around 80 deg. In the AP configuration (180 deg) T_c is instead larger than at 0 deg (parallel), as expected – something that is not visible in data since it was taken at a temperature where both P and AP arrangements were fully superconducting. While a non-monotonic angular dependence of T_c has been already observed in theory and experiments on FFS structures, this is the first case where this effect is observed in an FSF spin-valve.

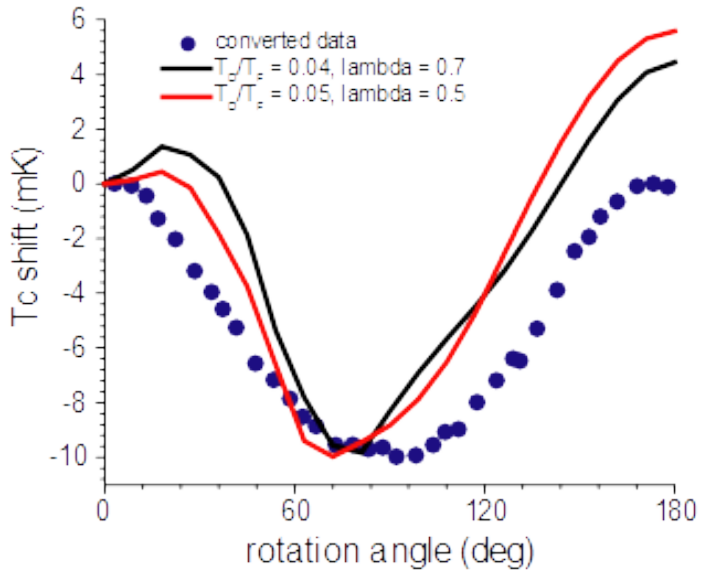

Fig. 8. Theory fits to the derived T_c shift from Fig.7 (right panel) for two sets of fit parameter (see text).